Materials Science & Engineering A 966 (2026) 150364

Contents lists available at ScienceDirect

Materials Science & Engineering A

journal homepage: www.elsevier.com/locate/msea

Tensile behavior at cryogenic temperatures of Al 7075 + 1.8%wt Zr alloy processed by L-PBF

Gabrielle Tiphéne [a,*], Nicolas Nothomb [a], Marie-Noëlle Avettand-Fénoël [b], Aude Simar [a,c]

[a] UCLouvain, IMMC (Institute of Mechanics, Materials and Civil Engineering), Louvain-la-Neuve, Belgium
[b] Univ. Lille, CNRS, INRAE, Centrale Lille, UMR 8207, UMET, Unité Matériaux et Transformations, F-59000 Lille, France
[c] WEL Research Institute, Wavre 1300, Belgium

ARTICLE INFO

Keywords:
L-PBF
Al 7xxx
Cryogenic temperature tensile testing

ABSTRACT

Additive manufacturing now enables the processing of high-strength Al 7xxx alloys through laser powder bed fusion (L-PBF). This work investigates the tensile behavior of an Al 7075 + 1.8%wt Zr alloy at room temperature and 77 K, addressing its potential for cryogenic applications. As-built specimens show moderate strength but maintain high ductility at both temperatures, whereas an optimized thermal treatment markedly improves strength, reaching a yield stress 680 MPa at 77 K, comparable to wrought Al 7075-T6. Modeling of thermally activated strengthening mechanisms provides results consistent with experimental findings, supporting the interpretation of strengthening contributions. Postmortem analysis confirms ductile fracture mode in all samples, with temperature and thermal treatment exerting limited influence on failure mechanisms. These results highlight the potential of L-PBF-processed Al 7xxx alloys for demanding structural applications requiring high strength at cryogenic temperature.

1. Introduction

Aerospace components face extreme space environments – low temperatures, thermal cycling, and vacuum – demanding high-performance materials for structural integrity and reliability. To cut mission costs and environmental impact, lightweighting is essential. The development of additive manufacturing (AM) technologies has enabled engineers to create more efficient, lightweight structures that were previously impossible or impractical to manufacture using traditional methods. AM allows for complex geometries and topology optimization, leading to further weight reduction and improved performance while maintaining the necessary strength and durability for space missions [1–4].

Additively manufactured materials exhibit unique microstructures and properties compared to conventional materials [5]. For space applications, characterizing these properties under operational conditions is critical. Recent studies have begun exploring low-temperature behavior in L-PBF materials, including steels [6], high-entropy alloys [7–9], titanium alloys [10,11] and aluminum alloys [12,13].

The 7xxx series of high-strength aluminum alloys is widely used in aerospace due to its excellent mechanical properties in harsh environments [14–20]. For example, Al 7075 in the T6 state can achieve a yield stress of 600 MPa at 77 K [19], making it particularly attractive for applications where the density-to-yield-stress ratio at low temperature is critical. However, the cryogenic deformation behavior of aged 7xxx alloys remains complex and poorly understood. Literature reports conflicting trends: some studies show reduced ductility at 77 K, while others observe improved elongation or non-monotonic temperature effects [17,21,22]. These inconsistencies arise from variations in initial temper conditions, particularly between naturally and peak-aged states. At low temperatures, three key mechanisms enhance ductility: suppression of the Portevin–Le Chatelier effect due to reduced solute atom mobility [23,24], activation of multiple slip systems improving deformation homogeneity [25] and enhanced work hardening through uniform dislocation cell structures [26–28].

Despite these advances, conventional wrought Al 7075 remains challenging to process via L-PBF due to hot cracking [29]. Recent advances demonstrate that eutectic-promoting elements (e.g., Si [30,31]) or grain refiners (AlTiB [32], TiC [33], Zr/Sc [34–39]) can mitigate this issue. For instance, AlZnMgCu + TiC + TiH2 leads to ultimate tensile stress (UTS) of 600 MPa at room temperature in T6-state [40] (550–650 MPa for conventional Al 7075-T6 [15,41,42]). AlZnMgCu + Sc + Zr leads to even higher UTS (near 650 MPa) after solution treatment and aging [39], thanks to $Al_3(Sc_xZr_{1-x})$ and η' nano-precipitates. As Sc is rare and quite expensive, Nothomb and al. [43,44] focus their interest on the L-PBF-processed Al 7075 + 1.8% Zr. After optimizing the processing parameters to process this alloy, they proposed a heat treatment

* Corresponding author.
E-mail address: gabrielle.tiphene@uclouvain.be (G. Tiphéne).

https://doi.org/10.1016/j.msea.2026.150364
Received 2 February 2026; Received in revised form 16 April 2026; Accepted 4 May 2026
Available online 9 May 2026

Table 1
ICP analysis of the used powder, reference wrought Al 7075 and L-PBF-processed samples (in %wt).

	Al	Cr	Cu	Fe	Mg	Si	Zn	Zr
Wrought Al 7075	bal.	0.18	1.51	0.08	2.55	0.04	5.93	–
Powder mix	bal.	0.22	1.56	0.08	2.48	0.02	5.36	1.86
L-PBF processed samples	bal.	0.22	1.52	0.08	1.73	0.03	3.27	1.84

leading to promising static mechanical properties at room temperature (UTS 540 MPa). However, cryogenic performance of these L-PBF alloys remains unexplored, despite their distinct microstructures (e.g., fine grains, metastable phases) compared to wrought counterparts. This study addresses this gap by evaluating the low-temperature mechanical behavior of L-PBF-processed Al 7075 + 1.8% Zr, a cost-effective alternative to Sc-modified alloys [39,43–45].

2. Materials and methods

2.1. L-PBF process

The Al 7075 + 1.8%wt Zr powder used in this work is identical to the one developed by [44,46]. The L-PBF process utilized a ProX® DMP 200 equipment (3D Systems Inc., USA), with a laser operating at a wavelength of 1075 nm, a 70 μm spot size and a maximum power of 273 W. Samples were manufactured on a non-heated Al5Mg build plate, measuring 141 mm × 141 mm × 25 mm. All samples were processed using the pre-sintering strategy proposed by [44,46], optimized for this powder. Plate-like samples of dimensions 70 mm × 30 mm × 1.5 mm were processed under argon gas keeping the chamber below 500 ppm of O_2, using a laser power of 164 W, a scanning speed of 400 mm/s, a hatching space of 50 μm and a layer thickness of 30 μm. The scanning pattern is composed of 5000 μm side regular hexagon with 100 μm overlapping between adjacent hexagons.

After L-PBF, the plates underwent thermal treatment in a Muffle furnace Nabertherm 1100°C. Heat treatments (HT) at 425°C for 1 h followed by water quenching and natural aging (NA) were applied [43,44]. No artificial aging was performed because it produces only a small amount of hardening precipitates in that alloy [44]. Samples were polished to reduce roughness caused by printing. A wrought sheet of Al 7075 in the T6 state was machined to produce comparison samples. Some samples, named T4, were thermally treated at 470°C for 1 h followed by water quenching and natural aging. Heat treatment at 470°C for 1 h of the L-PBF processed samples was also performed but is not the main focus of the present manuscript. The corresponding results can be found in the Supplementary III.

ICP-OES analyses were performed on the powder, L-PBF-processed samples and reference material using an Agilent Technologies 5100 ICP-OES equipment. The chemical composition obtained from these analyses is provided in Table 1. Clear evaporation of Zn and Mg is generated by L-PBF processing, as discussed by [43,44,46].

2.2. Characterization techniques

Tensile tests were carried out on a Zwick Roell Z50 device at 1 mm/min, at both RT and 77 K [47,48]. An MTS axial extensometer with a gauge length of 18.8 mm was used. The setup was immersed in a liquid nitrogen bath for at least 10 min before testing inside the bath. No temperature variation were observed during the tests. Details of the setup may be found in Supplementary SI. The tensile tests were performed with the loading axis perpendicular to the build direction. The initial cross-sectional area S_0 of each sample was measured using an Abbe Comparator Model B. The final cross-sectional area S_f was measured optically using a Keyence VHX-7000 optical microscope and analyzed with PlotDigitizer [49]. The yield stress σ_y, the ultimate tensile stress σ_{UTS} and the ultimate uniform deformation ε_u were extracted from the true stress-true strain curves. The fracture strain ε_f was determined post-mortem and calculated as [50]:

$$\varepsilon_f = \ln\left(\frac{S_0}{S_f}\right) \tag{1}$$

To balance L-PBF-processed sample availability with statistical rigor, the testing protocol was structured as follows. Room-temperature tensile tests included only one confirmation test per condition (AB, heat-treated), as existing RT data for this alloy [44] provided a reference baseline and sample resources were prioritized for cryogenic evaluation where variability was anticipated. Cryogenic (77K) tests, by contrast, involved multiple specimens (at least 4) per condition to ensure robust statistical analysis.

To further verify the homogeneity of mechanical properties in L-PBF-processed samples, Vickers hardness measurements were performed using a DuraScan G5 indentor (EmcoTest, Austria). To achieve the most consistent maximum depth possible, HV0.2 or HV0.1 were applied depending on the samples. Using a dwell time of 10 s, 50 indents per sample were conducted on four samples from each series for statistical accuracy.

To analyze the microstructure, the samples were mechanically polished to a mirror finish before finished with OPS. The microstructure was characterized using backscattered electron detector in a scanning electron microscope FEG-SEM Ultra55 (Zeiss). Energy-dispersive X-ray spectroscopy (EDX) analysis was performed using a Brucker XFlash 5010 detector. 10 h-maps as well as point spectrum were acquired to identify precipitates. Electron Back-Scattering Diffraction (EBSD) was used for further analyze of the microstructures of as-built (AB) and HT 1 h 425°C + NA samples. Post-processing of the obtained data was performed using the MTEX MATLAB Toolbox [51]. To categorize grains, they are approximated to ellipse with L the long and w the small axis. The aspect ratio AR is then defined as AR = L/w. To estimate their diameter ϕ, they are assumed to be spherical so $\phi = 2\sqrt{A/\pi}$. Grains are categorized into fine equiaxial grains (diameter $\phi < 2\,\mu m$), columnar grains (aspect ratio AR > 3 and diameter $\phi > 2\,\mu m$) and medium equiaxial grains (aspect ratio AR < 3 and diameter $\phi > 2\,\mu m$).

X-ray tomography analysis was performed on an EasyTom XL system to quantify defects and porosity levels in samples extracted from the grip sections of the as-built and heat-treated tensile test specimens, ensuring identical processing history for direct comparability. The resulting images had an isotropic voxel size of 1 μm^3. For each condition, four samples were analyzed using the same measurement volume to ensure consistency. Porosity analysis was conducted with Fiji [52] and Avizo software, where the equivalent diameter of pores was calculated from their detected volumes under the assumption of spherical morphology.

3. Results

3.1. Tensile tests

True stress–true strain curves at RT and 77 K are plotted in Fig. 1, with the corresponding engineering stress–strain curves provided as Supplementary SIII. A summary of all tensile results is provided in Table 2. As expected from the results of [44], the AB sample shows lower mechanical properties (yield stress and ultimate tensile stress) at RT compared to wrought Al 7075 in the T6 state. However, thermal treatments improve the yield and ultimate tensile stress levels of the L-PBF processed material, surpassing those of the wrought T4 samples and approaching those of the wrought T6 alloy. Despite this improvement, L-PBF-processed samples exhibit reduced ductility at RT compared to the wrought Al 7075. Heat treatments do not significantly affect the ductility of these samples. In the L-PBF samples, a Lüders plateau is observed after the yield stress is reached, as in [43,44]. A strong Portevin–Le Chatelier (PLC) effect is observed in the AB state but disappears after heat treatment [43,44,53].

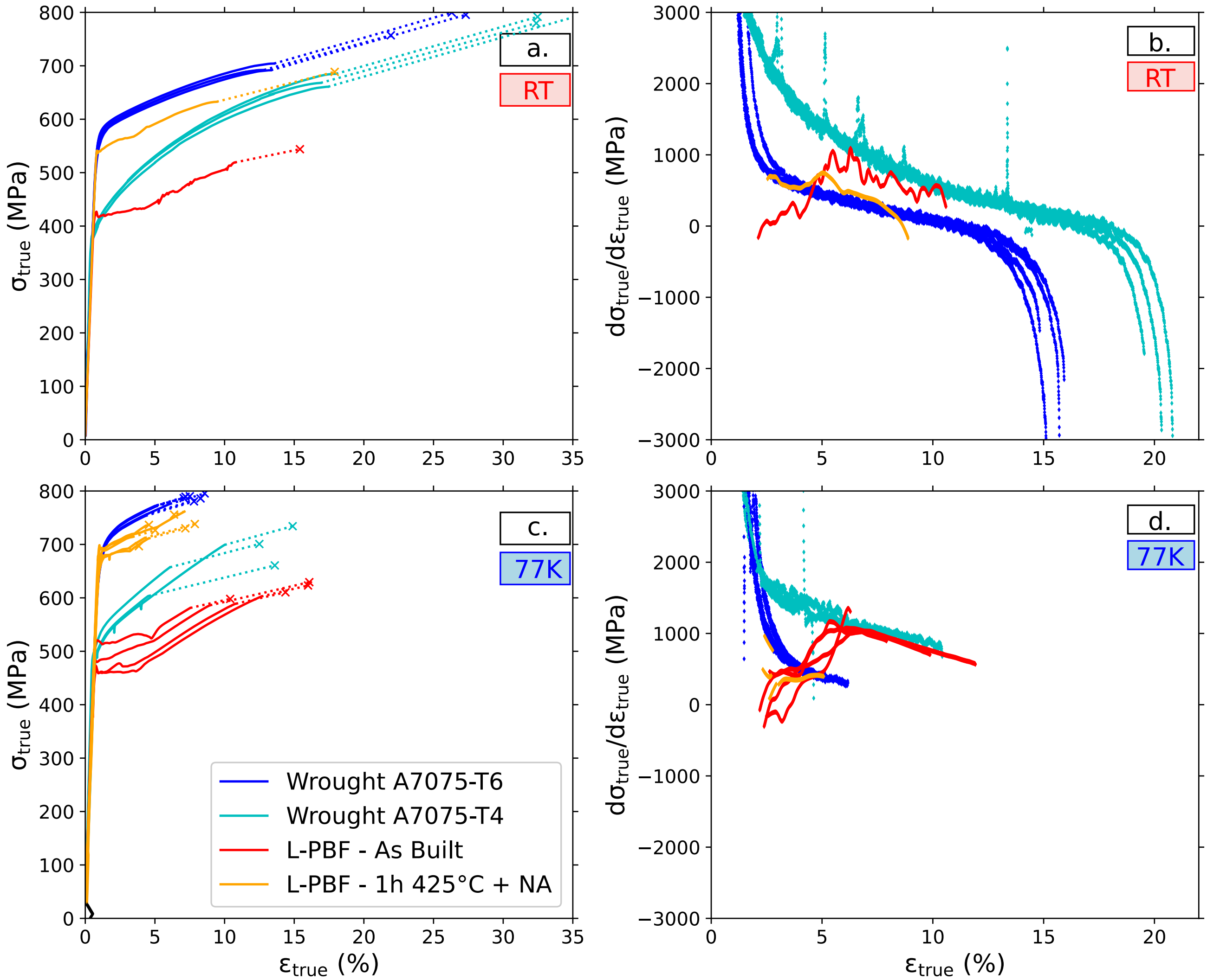

Fig. 1. True stress versus true strain curves for the Al 7075 + 1.8%wt Zr alloy tested at RT (a) and 77 K (c) are shown. (b) and (d) present the corresponding hardening rate (mean value on 400 data points). AB samples exhibit relatively low stress values for a high-strength aluminum alloy while heat treated ones show promising properties. After Lüders plateau, the hardening rate of the AB sample is similar to the one of sample in T4 state and 1 h 425°C + NA has an hardening rate following the one of the T6 state. The low ductility of heat-treated samples at 77K complicates the analysis.

Table 2
Tensile results obtained at RT and 77 K for Al 7075 + 1.8%wt Zr samples subjected to various thermal treatments.

Condition	σ_y (MPa)		σ_{UTS} (MPa)		ε_u (%)		ε_f (%)	
	77 K	RT	77 K	RT	77 K	RT	77 K	RT
Al 7075-T6 [41,42]	–	≈ 550	–	550 – 650	–	≈ 10	–	–
Al 7075-T6 [19]	600	523	660	570	7.3	12	7.3	15.2
Scalmalloy [12]	545	384	583	404	3	9	–	–
Al 7075-T6	666 ± 4	558 ± 6	764 ± 11	696 ± 7	5.0 ± 0.8	13.2 ± 0.5	7.9 ± 0.7	22.1 ± 8.2
Al 7075-T4	499 ± 9	369 ± 8	653 ± 48	671 ± 12	6.9 ± 2.8	17.4 ± 0.6	13.7 ± 1.2	34.8 ± 4.0
AB	480 ± 25	423	589 ± 10	519	10.0 ± 2.2	10.7	14.2 ± 2.7	15.4
HT 470 °C 1 h + NA	634 ± 39	538	706 ± 48	582	7.2 ± 1.7	7.9	9.6 ± 2.2	16
HT 1 h 425°C + NA	680 ± 14	535	719 ± 28	633	4.2 ± 1.9	9.4	5.8 ± 1.6	17.9

At 77 K, the AB samples show low stress levels compared to the wrought alloy but maintain similar ductility compared to the RT sample. Cryogenic temperatures reduce the ductility of heat treated samples while increasing their yield stress. The HT 1 h 425°C + NA condition achieves yield stress comparable to the reference wrought T6 material but still exhibits lower ductility. Significant variability in the reached yield and ultimate stress levels is observed at 77 K for the L-PBF processed samples. The PLC effect observed at RT on the AB sample has disappeared at 77K. On the contrary, Lüders plateau seems more pronounced compared to RT in this state (Supplementary III). For the heat treated sample, Lüders plateau decreases with temperature.

Rate hardening are calculated for the different samples at both RT and 77K (see Fig. 1b and d). The data for the L-PBF-manufactured samples are highly noisy due to the Lüders plateau and the PLC effect. A moving average (over 400 points) was therefore applied before calculating the strain hardening rate. As expected, the T4 state presents a higher rate compared to the one of the T6 state. After the end of Lüders plateau (up to 3 to 5% deformation), the AB state samples have

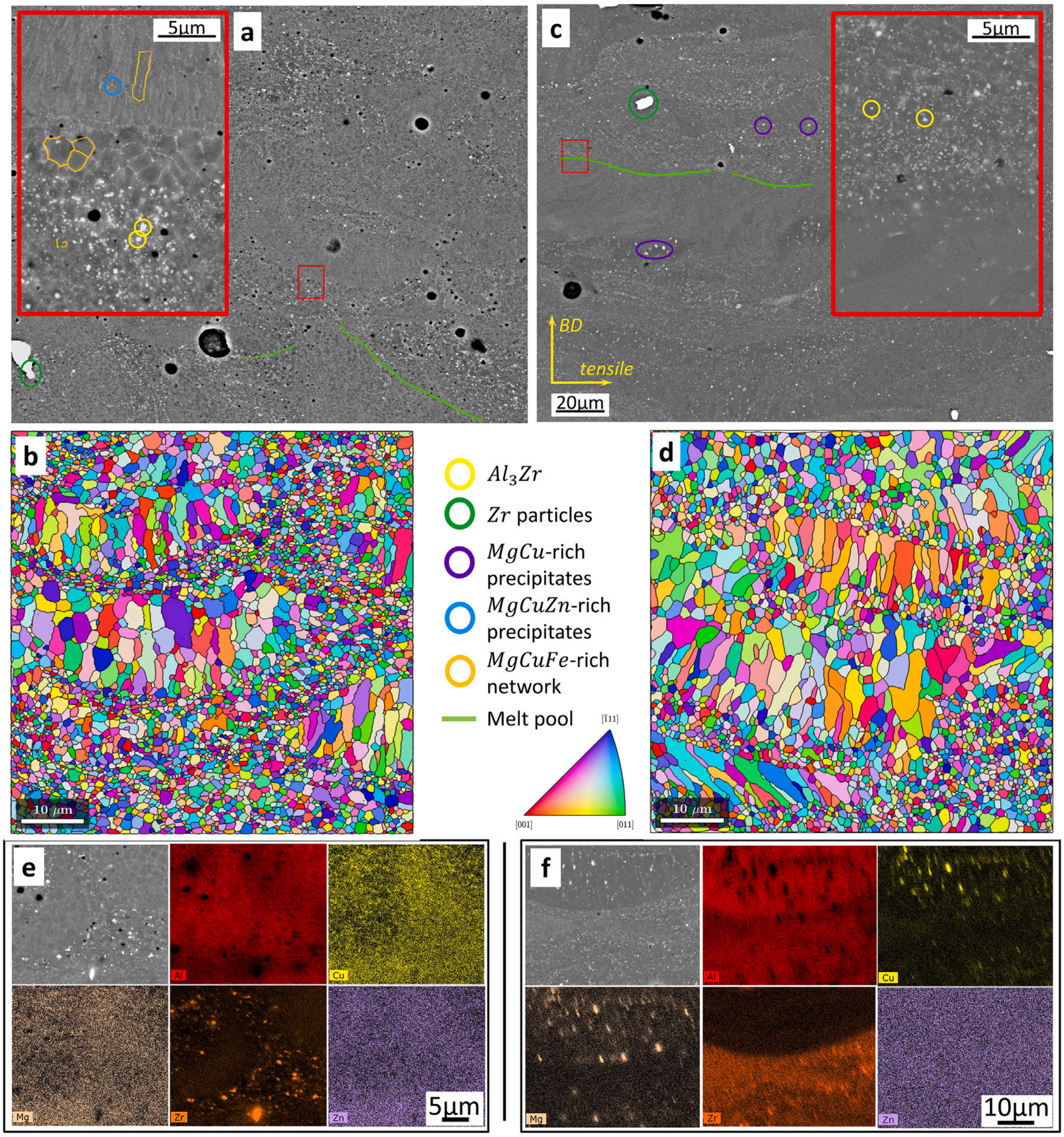

Fig. 2. SEM observation of the microstructure of (a) AB and (c) HT 1 h 425°C + NA. EBSD maps for (b) AB and (d) HT 1 h 425°C + NA. Porosity is shown in black and precipitates in white (a and c). EDX maps of (e) AB and (f) HT 1 h 425°C + NA (X-ray emission lines: Cu $K\alpha$, Cr $K\alpha$, Mg $K\alpha$, Zn $K\alpha$, Zr $K\alpha$). In the AB state, Zr-based precipitates, likely Al_3Zr are observed. Mg, Cu and Zn appear heterogeneously distributed, mainly in the fine-grain zone and the precipitate network at the grain boundaries appears rich in Cu, Mg and Zn. In the heat-treated state, Zn precipitates seem to have dissolved. Cu-Mg-based precipitates are visible in the large-grain zones, while Zr precipitates are detected in the small equiaxed grain zones [44]. These distributions are consistent with TEM observations in [44]. Semi-quantitative identification of precipitates may be found in Supplementary V. (For interpretation of the references to color in this figure legend, the reader is referred to the web version of this article.)

an hardening rate similar to the T4 samples. At the opposite, the 1 h 425°C + NA sample seems to follow the trend of the T6 samples. There is no clear effect of the temperature on the hardening rate.

Young's modulus values were estimated from those tensile curve. It gives 68 ± 1 GPa at RT and 74 ± 8 GPa at 77 K for the L-PBF processed samples, matching pure aluminum expectations (70 GPa at RT and 78 GPa at 77 K) [54].

3.2. Microstructure

Fig. 2 presents the microstructure of AB and HT 1 h 425°C + NA samples. In the AB state (Fig. 2a. and b.), melt-pools with elongated grains at the center and equiaxed grains at the border are visible. Large Zr particles and rounded pores are observed. A continuous network of precipitates is detected along the grain boundaries (Fig. 2a., highlighted in gold in the sub-figure). Submicron precipitates were observed (Sky blue), as well as square-like precipitates (yellow), likely Al_3Zr [43,44]. No non-spherical pores were detected, contrary to previous reports on this material [44,46].

Heat-treated samples (Fig. 2c. and d.) retain the bimodal distribution while showing reduced porosity. Thermal treatment dissolved the continuous precipitate network. Micron-size precipitates are now detected (Fig. 2c., highlighted in purple).

EDX maps (Fig. 2e. and f.) and semi-quantitative analysis (Supplementary V) allows identification of micron-size precipitates. The small square-shaped precipitates were identified as Zr-based ones, likely Al_3Zr grain refiners [37,44,56]. In the AB state, MgCuFe-rich and MgCuFeZn-rich precipitates were detected, while in HT samples,

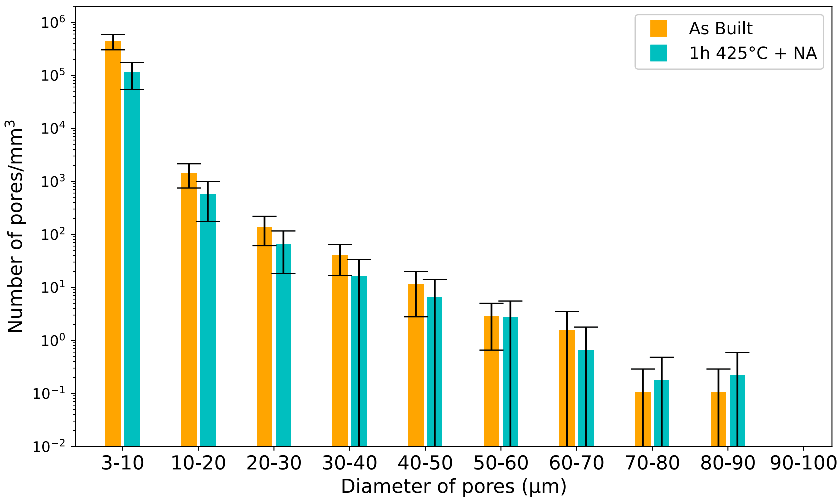

Fig. 3. Porosity distribution in log scale as a function of equivalent diameter in the AB and HT 1 h 425°C + NA states, from the X-ray tomography data analysis. For statistics, 4 samples were analyzed for each condition (Supplementary II). A reduction of porosity is resulting from the thermal treatment [55]. Since not all four analyzed samples present large pores (d > 60 µm), the standard deviations obtained are significant.

Table 3
EBSD analysis and tomography results of the AB and HT 1 h 425°C + NA samples.

	AB	HT 1 h 425°C + NA
Porosity fraction voxel size = $1\,\mu m^3$	0.7%	0.1%
Fine grains $\phi < 2\,\mu m$	$\phi_{eq} = 0.7 \pm 0.4\,\mu m$	$\phi_{eq} = 1.0 \pm 0.4\,\mu m$
Medium grains $\phi > 2\,\mu m$ $AR < 3$	$\phi_{eq} = 2.6 \pm 0.7\,\mu m$	$\phi_{eq} = 2.6 \pm 0.7\,\mu m$
Columnar grains $\phi > 2\,\mu m$ $AR > 3$	$L = 5.1 \pm 1.5\,\mu m$ $w = 1.4 \pm 0.2\,\mu m$ $\phi_{eq} = 2.7 \pm 0.5\,\mu m$	$L = 6.1 \pm 2.4\,\mu m$ $w = 1.7 \pm 0.6\,\mu m$ $\phi_{eq} = 3.2 \pm 1.1\,\mu m$
Fine grains area fraction (%)	71	69
Medium grains area fraction (%)	27	27
Columnar grains area fraction (%)	2	4

Table 4
Vickers hardness and the corresponding representative stress σ_r [57], measured at RT, for Al 7075 + 1.8%wt Zr and Al 7075 in T6 state samples. In all cases, ε_r is calculated to be 9.1–9.4% of deformation, as expected for Vickers hardness [57].

Sample	Al 7075 - T6		AB		HT 1 h 425°C + NA	
	HV0.2	σ_r (MPa)	HV0.1	σ_r (MPa)	HV0.2	σ_r (MPa)
1	175 ± 2	680 ± 8	116 ± 7	437 ± 25	160 ± 6	617 ± 22
2	178 ± 2	690 ± 9	120 ± 10	454 ± 37	162 ± 7	624 ± 25
3	178 ± 2	692 ± 8	127 ± 9	483 ± 33	159 ± 6	613 ± 21
4	178 ± 3	693 ± 11	125 ± 7	472 ± 25	157 ± 14	602 ± 50
Mean value	177 ± 1	688 ± 5	122 ± 4	460 ± 25	159 ± 2	614 ± 8

MgCuFe-rich and MgCu-rich precipitates were found [44]. Zn is expected to be in solid solution after the heat treatment [44].

Using EBSD analysis (Fig. 2b. and d.), grains were categorized into fine grains, columnar grains and medium grains, as described in [44]. The results are presented in Table 3. Grain sizes match previous reports, with some variation in medium and large grain fraction [44].

Porosity detection was conducted using X-ray tomography. Mean porosity distributions across diameter ranges (log scale) are compared in Fig. 3, while individual results are provided in Supplementary SII. A clear decrease in porosity content with increasing pore diameter is observed for all conditions. Furthermore, the heat treatment reduces porosity levels compared to the AB state. This likely improving mechanical properties by minimizing stress concentration zones associated with pores [55]. Since there are fewer than one pore with a diameter greater than 60 µm per mm^3, their presence is likely attributable to sample processing.

4. Discussion

4.1. Stress dispersion in tensile tests

Fig. 1 shows notable variability in 77 K stress levels among L-PBF samples. To distinguish setup from sample effects on this variability, three K-type thermocouples where added to the setup and confirmed stable 77 K conditions within 2 min. Vickers hardness (RT) was measured on four samples per condition to assess heterogeneity (results in Table 4). Assuming material homogeneity under the indents, representative stress σ_r and strain ε_r can be derived from Vickers hardness measurements using Young's modulus E [57]:

$$\sigma_r = \frac{\xi_3 \cot(\theta)}{\xi_1 \cot(\theta) - (1 - \xi_2) H/E} H \tag{2}$$

$$\varepsilon_r = (1 - \xi_2)\frac{\sigma_r}{E} + \xi_3 \cot(\theta) \tag{3}$$

with H the hardness of the sample, θ the conical equivalent angle of the indenter [57] and ξ_1, ξ_2 and ξ_3 constants depending on the indenter angle [57]. This analysis determines the point $(\varepsilon_r, \sigma_r)$ on the stress–strain curve, with $\varepsilon_r \approx 8 - 10\%$ for a Vickers indenter [57].

L-PBF samples show significant hardness variability compared to wrought Al 7075-T6 (Table 4). Representative stress matches RT values at 9% deformation, with 10–20 MPa dispersion, reflecting the 77 K stress variability. Representative stress orders of magnitude align with ultimate tensile stress. This consistency suggests the observed stress–strain variability is intrinsic to the samples. Aluminum's thermal sensitivity in L-PBF suggests printing position on the platform as well as samples' geometry may drive these variations [58–62]. This effect also accounts for the microstructural (Fig. 2) and hardness differences (Table 4) as well as absence of lack-of-fusion pores, compared to [44]. Here, the sample geometry (walls versus cubes) increases the processing temperature compared to [44], reducing thermal gradients which promote the formation of Al_3Zr and the growth of equiaxed grains [63, 64] and modifies the microstructure and mechanical properties.

Sample heterogeneity likely stems from microstructural variability; indents (10 µm depth, ≈ 100 µm tested radius [65]) exceed individual grain size. Results reflect mixed fine/coarse-grained regions with uneven porosity. Since porosity lowers hardness and is heterogeneously distributed, hardness and stress vary significantly across indentations on the same sample.

4.2. Strengthening mechanisms at low temperature

For this alloy, following the work of Nothomb et al. [44], σ_y may be decomposed in :

$$\sigma_y(T) = \sigma_{fric}(T) + \sigma_{GB}(T) + \sigma_{BS}(T) + \sigma_{SS}(T) + \sigma_{PS}(T) \tag{4}$$

with σ_{fric}, σ_{GB}, σ_{BS}, σ_{SS} and σ_{PS} the contribution of the lattice friction, the grain boundaries, the back-stresses, the solution strengthening and the precipitates strengthening, respectively. The porosity level measured here is low, so no impact of pores on the yield stress is expected. As the microstructure is heterogeneous, a mixture law is applied on each term, as in [44]:

$$\sigma_{mechanism}(T) = f_{fine}\sigma^{fine}_{mechanism}(T) + f_{medium}\sigma^{medium}_{mechanism}(T) + f_{columnar}\sigma^{columnar}_{mechanism}(T) \tag{5}$$

where *mechanism* correspond to the strengthening mechanisms considered here, the grain fractions f are determined from the EBSD maps (Table 3).

To account for temperature effects, each contribution's temperature dependence is modeled. The temperature-dependent yield stress is given by [66–68]:

$$\sigma_y(T) = \sigma^*(T) + \sigma^{th}(T) \tag{6}$$

where σ^* represents athermal stresses (long-range obstacles) and σ^{th} thermal stresses (short-range obstacles). Thermal stresses decrease significantly with increasing temperature, while athermal stresses remain relatively constant.

Back stress and grain boundary contributions (Eq. (4)) are athermal [69], depending on long-range obstacles; other mechanisms are thermally activated [68,70–81]. Based on the model proposed by [44], the athermal stresses σ_{GB} and σ_{BS} are expressed as:

$$\sigma_{GB}(T) = k(T)\sqrt{\frac{b}{d}} \tag{7}$$

with b the Burger's vector, d the grain diameter and $k(T) = \beta\mu(T)$. β is calculated at RT knowing k at this temperature and the shear modulus μ [44].

$$\sigma_{BS}(T) = Mn\mu(T)\frac{b}{d} \tag{8}$$

with M the average matrix orientation factor of aluminum and n the number of dislocations in a pile-up (Table 5). As these two mechanisms are inversely proportional to grain size, they are expected to have a greater impact on strengthening in the AB samples compared to the 1 h 425°C + NA heat-treated samples. Moreover, for a given thermal treatment, since the shear modulus increases with decreasing temperature [54], this effect will also be enhanced at lower temperatures.

On the other hand, thermal stresses contribution may be expressed as [66–68]:

$$\sigma^{th}(T) = \sum_1^n \sigma_i(T) = \sum_1^n s_i(\dot{\varepsilon}, T)\frac{\mu(T)}{\mu(T = 0K)}\sigma_{0i} \tag{9}$$

with σ_{i0} the mechanical threshold stress of the thermally activated strengthening mechanism i. σ_{i0} can be seen as the stress to overcome the obstacle without thermal assistance i.e. at 0 K. s_i is the thermal activation term of strengthening mechanism i [67]:

$$s_i(\dot{\varepsilon}, T) = \left(1 - \left[\frac{k_B T}{g_{0i}\mu b^3}\log\left(\frac{\dot{\varepsilon}_{0i}}{\dot{\varepsilon}}\right)\right]^{1/q_i}\right)^{1/p_i} \tag{10}$$

Table 5
Parameters to compute strengthening contribution variations in temperature.

Symbol	Value	Unit	References	Remarks
ν	0.33	–	[37,39,44,82,83]	Constant in T
E	68	GPa	This work	RT
	74	GPa	This work	77 K
	78.1	GPa	[54]	0 K
μ	$\frac{E(T)}{2(1+\nu)}$	GPa	[84]	
β	0.39		Calculated from k(RT) [44]	Constant in T
b	0.286	nm	[37,39,44]	Constant in T
M	3.06	–	[37,39,44]	Constant in T
n	3	–	[44,85]	Constant in T
$\sigma_{friction}$	20	MPa	[39,44,86,87]	RT
γ	0	°	[79]	Constant in T
M_{Taylor}	3	–	[75]	

Table 6
Model parameters to compute the thermal activation term of strengthening mechanism i.

Mechanism	g_0	p	q	$\dot{\varepsilon}_0$ (/s)	Parameters from
Lattice friction	0.65	1/2	3/2	1e7	[67,88]
PS - Shear	1.57	2/3	1	1e7	[67,80]
PS - Orowan loops	Eq. (11)	1	3/2	1e7	[67,79,80]
Solution strengthening	$g_0(c_{solute})$	1	3/2	1e4	[72,73]

Table 7
Parameters to compute τ^{solute}_{i0} and ΔE_b, knowing the solute atomic concentration c.
Source: From [73].

Solute	$\tau^{solute}_{i0}/c^{2/3}$	$\Delta E^{solute}_b/c^{1/3}$ (eV)
Cr	705	6.65
Cu	348	4.10
Fe	1072	8.20
Mg	342	4.06

With k_B the Boltzmann's constant, T the temperature and $\dot{\varepsilon}$ the strain rate, taken at 10^{-2}/s here. The normalized activation energy g_{0i}, the strain rate $\dot{\varepsilon}_{0i}$, p_i and q_i are characteristic parameters, related to the strengthening mechanism (Table 6). For all these mechanisms, increasing the test temperature provides more thermal energy to overcome the corresponding obstacle. Since the total energy required to overcome the obstacle is assumed to remain constant, the energy contribution from the applied stress decreases as the test temperature rises.

Where literature values for σ_{0i} exist (only for solution strengthening [72,73]), $\sigma_i(T)$ was calculated at both RT and 77K. For other mechanisms, $\sigma_i(RT)$ was determined as per [44] before identifying σ_{0i}.

For Orowan precipitation strengthening, $g_{0Orowan}$ is defined as [79,80]:

$$g_{0Orowan} = \log(2R)\log(L)\log\left(\frac{2RL}{2R+L}\right)\frac{1-\nu\cos^2\gamma}{2\pi(1-nu)} \tag{11}$$

with R the precipitate radius, γ the angle between dislocations and the Burgers vector. The impact of γ value was calculated and is negligible in the present case.

$$L = 2R\left(\sqrt[3]{\frac{\pi}{6\phi}} - 1\right) \tag{12}$$

with ϕ the precipitates volume fraction.

Temperature-dependent solid solution strengthening was modeled using Leyson et al.'s approach [72,73], which builds on Follansbee et al.'s framework [67,68]. They provide τ^{solute}_{i0} and $\Delta E_b = g_{0i}\mu b^3$ as functions of solute concentration (Table 7). In the present analysis, the used atomic concentration may be found in Table 8.

$$\sigma^{solute}_{i0} = M_{Taylor}\tau^{solute}_{i0} \tag{13}$$

Table 8
Solute concentration in matrix considered in the model for AB and HT 1 h 425°C. Mean values are taken from EDX analysis, see Supplementary V.

	Cr (%at)	Cu (%at)	Fe (%at)	Mg (%at)	Zn (%at)	Zr (%at)
AB	0.12 ± 0.02	0.67 ± 0.04	0.04 ± 0.02	2.28 ± 0.16	1.02 ± 0.04	0.45 ± 0.03
HT 1 h 425°C	–	0.7 ± 0.04	–	–	1.1 ± 0.04	–
A7075 - T6	0.08 ± 0.02	0.54 ± 0.03	0.02 ± 0.01	3.52 ± 0.09	0.05 ± 0.01	2.09 ± 0.04

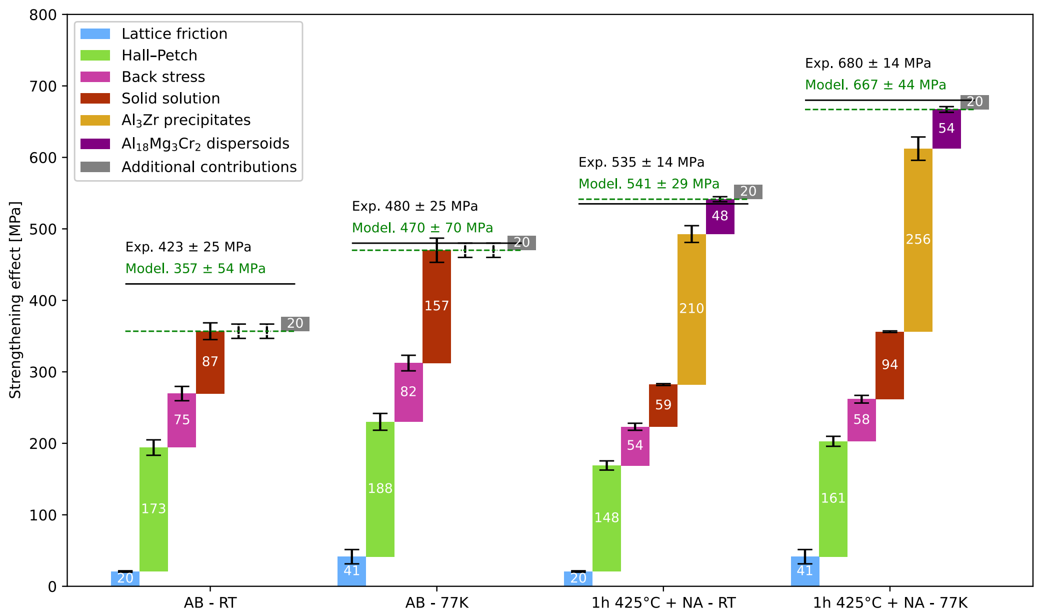

Fig. 4. Comparison of strengthening mechanism contributions at RT and 77K, computed for AB and HT 1 h 425°C + NA.

Ma et al.'s analysis [75] gives τ_{i0}^{Zn} and ΔE_b^{Zn} thermal dependence. For Zr-lacking data, we assumed: $\tau_{i0}^{Zr}/c(Zr)^{2/3} = \tau_{i0}^{Cu}/c(Cu)^{2/3}$ and $\Delta E_b^{Zr}/c(Zr)^{1/3} = \Delta E_b^{Cu}/c(Cu)^{1/3}$.

While micron/sub-micron Al_3Zr precipitates (visible in Fig. 2) act as inoculants for grain refinement during solidification, they are expected to contribute minimally to hardening due to their size and spacing. The model specifically targets nanometer-scale precipitates, which are the primary drivers of shear strengthening or Orowan strengthening. Secondary precipitates (Al_3Zr, AlMgCr) form during high-temperature heat treatment [44]. We assume that these secondary precipitates are not yet formed in the AB state, so nanoscale precipitate strengthening was not considered in this case.

HT 1 h 425°C + NA samples were heat-treated at high temperature, identically to the HT 1 h 425°C + AA samples in [44]. Nothomb et al. [44] clearly highlight that artificial aging does not lead to the formation of η and η' due to Mg/Zn depletion related to L-PBF processing. Moreover, AA at 120°C does not alter the Zr-based (Al_3Zr) or AlMgCr precipitate populations, which remain stable [89–93]. Thus, we use the same Al_3Zr and AlMgCr precipitate distributions and radii for the HT 1 h 425°C + NA samples. Those precipitate characteristics were identified by TEM in [44] and are shown in Supplementary VII. For Al_3Zr, the contribution are split between fine grain zone (R = 1.3 nm, ϕ = 0.65%) and coarse (medium and columnar) grain zone (R = 1.7 nm, ϕ = 1.24%). For the AlMgCr precipitates, R = 33 nm and ϕ = 1.4%. As in [44], only Cu and Zn contribute to solution strengthening; their solid-solution proportions are estimated from EDX maps (Supplementary V) and TEM analysis [44].

Fig. 4 details the contributions of each mechanism at RT and 77 K for both AB and HT 1 h 425°C + NA samples. The predicted increase in yield stress with decreasing temperature matches experimental observations. The obtained values are reasonably good for the heat-treated sample (less than 2% differences between the model and the experiment at both RT and 77 K) but more detailed analysis is required for the AB sample (15% difference at RT). For the heat-treated sample, the Al_3Zr precipitates provide the main strengthening contributions, at both tested temperatures.

The Hall-Petch effect and back-stress strengthening are more pronounced in the AB samples than in the heat-treated ones. This is consistent, as both phenomena depend directly on grain size and the AB samples exhibit smaller grains compared to the heat-treated samples.

For solid solution strengthening and precipitation strengthening, these mechanisms depend on the element distribution, which is controlled by the processing steps and heat treatment. Under the given hypotheses, it is consistent that solid solution strengthening is more significant in the AB samples than in the heat-treated ones.

As observed in the heat-treated sample, the thermal activation of solid solution strengthening and precipitation strengthening differs due to their distinct activation energies. Based on this effect and the results from the AB samples, it is highly probable that some atoms assumed to be in solid solution in AB instead form nanoscale hardening precipitates in those samples. It is expected to better explain the AB behavior. However, a more complex quantification would be required to investigate this further. Since the mechanical properties of this sample are not the primary focus of this article, it will not be here explored in greater depth.

Finally, the ICP analysis (Table 1) shows that the Mg and Zn content of the L-PBF-processed samples decreased due to evaporation during fabrication. This reduction in both elements likely impacted the solution strengthening effect. For comparison, when compensating for this evaporation and applying an optimized heat treatment [94], Al 7075 + 1.5% Zr can reach a hardness of 220 HV, significantly higher than the values obtained here with our optimized treatment or those of wrought Al 7075-T6.

4.3. PLC and Lüders's plateau

As explained in [44,53], the PLC effect arises from interactions between mobile dislocations and solute atoms. The high cooling rate

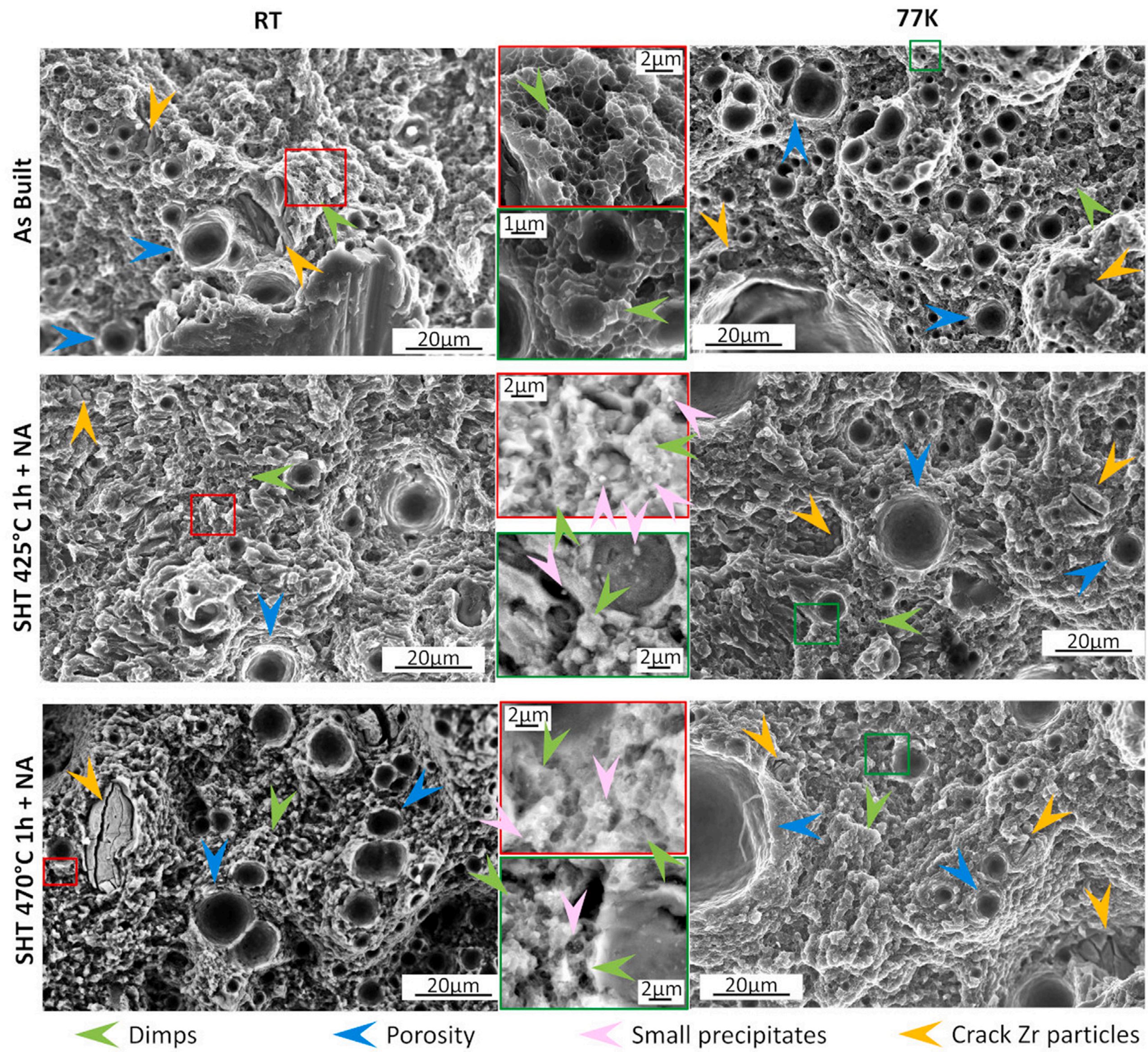

Fig. 5. Fracture surfaces after tensile testing at room temperature (left) and 77 K (right), observed by SEM (secondary electrons). In all cases, large fractured particles as well as dimples and porosity are visible beneath the fracture surface. All specimens present a ductile fracture.

of the L-PBF process traps a high amount of solute atoms in the AB samples. Heat treatment at 425°C enables atomic diffusion and thus formation of precipitates, thereby reducing the proportion of these trapped solute atoms. This mechanism aligns with the observed decrease and disappearance of the PLC effect in the HT 425°C samples.

With temperature decreasing to 77K, the PLC effect disappears at lower temperatures — consistent with observations in Al-Mg alloys [19,23,95,96]. Yu et al. [97] attribute PLC serration disappearance at lower temperatures to grain size dependence in ultrafine-grained aluminum: for a fixed microstructure, the critical grain size for PLC effects decreases with temperature, explaining their absence at 77 K. Solute atoms (such as Mg) pin dislocations, intensifying PLC effects [23]. Since atomic diffusivity in Al decreases at lower temperatures [19,95,98], fewer atoms migrate to dislocations at 77 K, reducing or eliminating PLC phenomena.

Lüders plateau, observed after yield point, corresponds to the propagation of deformation bands [44]. This effect stems from the hindrance of initial dislocation motion by Cottrell atmospheres of solute atoms. Such behavior occurs in Al-Mg alloys [99–101], high-strength Al alloys [39,102–104] and low-carbon steels [105–108].

In the present study, Lüders plateau extent increases with decreasing temperature for the AB samples. Tsuchida et al. observed similar behavior in low-carbon steels [105,109], though no clear explanation exists for this trend. Such behavior has also been observed with increasing strain rate testing at RT (for low strain rate $\dot{\varepsilon} < 10^3$) before reaching a saturation plateau [109]. Such behavior reminds the equivalence between time and temperature observed for creep for instance [110], but a more detailed analysis is beyond the scope of this paper.

HT reduces porosity in L-PBF samples (Figs. 2 and 3), consistent with Luo et al. [55]. Such effect is likely healing of the samples, due to Mg diffusion [111–113]. This porosity healing may also enhance ductility after HT.

4.4. Fracture mechanisms

Fracture surface analysis (Supplementary SIV) reveals deformation mechanisms: at RT, fracture occurs at 45° to the tensile direction, indicating void-sheet mechanism, while at 77 K, it is perpendicular (internal necking) [114,115]. Regardless of temperature, fracture surfaces show fractured Zr particles, pores and dimples (Fig. 5), with small precipi-

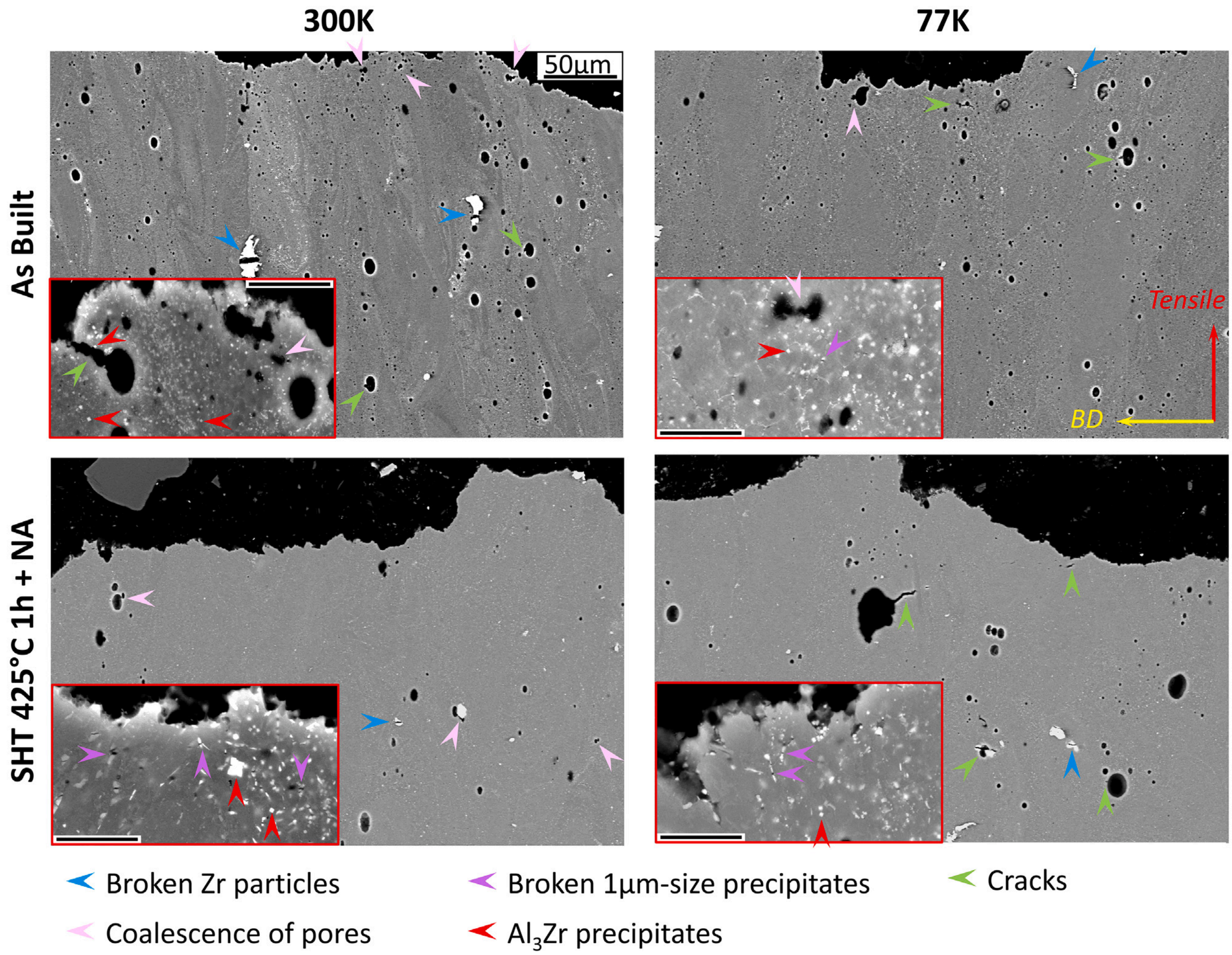

Fig. 6. Fracture surfaces observed after tensile testing at RT (left) and 77 K (right). In all cases, large fractured particles are visible beneath the fracture surface. All main images share the same scale bar, while the inset scale bar represents 5 µm.

tates inside dimples — consistent with Fig. 2. There is no clear effect of testing temperature nor heat-treatment on the fracture surface. Fig. 6 compares polished samples below the fracture surface after tensile tests at both temperatures. Fractured Zr particles remain well-bonded to the Al matrix in all samples. AB samples show cracks initiating near pores, while thermally treated samples also exhibit cracked small precipitates near the fracture surface — suggesting higher stress levels, in line with tensile results. No significant differences in fracture mechanisms are observed between temperatures or annealing conditions.

Regardless of damage mechanisms, this alloy (Al 7075 + 1.8%wt) demonstrates superior static properties at both RT and 77 K compared to L-PBF processed Scalmalloy [12]. The HT 1 h 425°C + NA treatment achieves a yield stress of 680 MPa at 77 K with 5.8% deformation, outperforming HIP-treated Scalmalloy (545 MPa, 3% deformation). A careful comparison between these alloys is required, as their deformation mechanisms may differ — particularly due to variations in thermal treatment and hardening mechanisms. These results highlight the potential of Al 7075 + 1.8% Zr for low-temperature applications, though further fatigue analysis at 77 K is needed.

5. Conclusions and perspectives

This study has evaluated the mechanical properties of L-PBF Al 7075 + 1.8 wt% Zr at 77 K, yielding the following key insights:

- Yield stress increases with decreasing temperature, while fracture strain decreases.
- AB samples exhibit lower tensile properties (25% lower yield and ultimate tensile stress) compared to wrought Al 7075 (T4/T6).
- Post-treatment improves tensile behavior at both RT and 77 K, achieving yield stress comparable to wrought Al 7075-T6 and surpassing L-PBF Scalmalloy [12].
- No significant differences are observed between temperatures or annealing conditions in fracture mechanisms.
- The temperature-dependent strengthening model aligns well with experimental results and highlight the different thermally-activated contributions.

To optimize performance, further characterization of printing direction and surface roughness effects is essential. Additionally, addressing Mg and Zn depletion-critical for hardening in 7xxx alloys [44], could enhance stress levels.

CRediT authorship contribution statement

Gabrielle Tiphéne: Writing – original draft, Visualization, Methodology, Investigation, Formal analysis, Data curation, Conceptualization. **Nicolas Nothomb:** Writing – review & editing, Resources, Methodology, Conceptualization. **Marie-Noëlle Avettand-Fénoël:** Writing – review & editing, Investigation, Data curation. **Aude Simar:** Writing

– review & editing, Supervision, Resources, Project administration, Methodology, Funding acquisition, Conceptualization.

Declaration of Generative AI and AI-assisted technologies in the writing process

During the preparation of this work the authors used Le Chat, an AI assistant developed by Mistral AI in order to correct for grammar and language accuracy. After using this tool, the authors reviewed and edited the content as needed and take full responsibility for the content of the published article.

Funding

The present research is funded by the Space4ReLaunch project, which is supported by the SPW Economie Emploi Recherche of the Walloon Region, under the grant agreement nr 2210181. The authors acknowledge the financial support from the Wallinov GreenAl project (convention n° 2310011) funded by the Service Public de Wallonie, Economie Emploi Recherche (SPW-EER), Belgium.

Declaration of competing interest

The authors declare that they have no known competing financial interests or personal relationships that could have appeared to influence the work reported in this paper.

Acknowledgments

The authors would like to thank the members of the LACAMI and LEMSC platforms for their technical support. The authors also wish to thank Olivier Poncelet and Camille van der Rest for their assistance with L-PBF processing. The authors would like to thank Mohammed Farag for his help in analyzing the tomography data as well as Pr. Pascal Jacques for his valuable time in conducting the EBSD experiments. Finally, the authors would like to thank Matthieu Lezaack for fruitful discussions on Al 7075.

Appendix A. Supplementary data

Supplementary material related to this article can be found online at https://doi.org/10.1016/j.msea.2026.150364.

Data availability

Data will be made available on request.

References

[1] B. Blakey-Milner, P. Gradl, G. Snedden, M. Brooks, J. Pitot, E. Lopez, M. Leary, F. Berto, A. du Plessis, Metal additive manufacturing in aerospace: A review, Mater. Des. 209 (2021) 110008, http://dx.doi.org/10.1016/j.matdes.2021.110008.

[2] T. DebRoy, H.L. Wei, J.S. Zuback, T. Mukherjee, J.W. Elmer, J.O. Milewski, A.M. Beese, A. Wilson-Heid, A. De, W. Zhang, Additive manufacturing of metallic components – Process, structure and properties, Prog. Mater. Sci. 92 (2018) 112–224, http://dx.doi.org/10.1016/j.pmatsci.2017.10.001.

[3] G. Liu, X. Zhang, X. Chen, Y. He, L. Cheng, M. Huo, J. Yin, F. Hao, S. Chen, P. Wang, S. Yi, L. Wan, Z. Mao, Z. Chen, X. Wang, Z. Cao, J. Lu, Additive manufacturing of structural materials, Mater. Sci. Eng.: R: Rep. 145 (2021) 100596, http://dx.doi.org/10.1016/j.mser.2020.100596.

[4] Y. Qi, Z. Hu, H. Zhang, X. Nie, C. Zhang, H. Zhu, High strength Al–Li alloy development for laser powder bed fusion, Addit. Manuf. 47 (2021) 102249, http://dx.doi.org/10.1016/j.addma.2021.102249.

[5] H.R. Kotadia, G. Gibbons, A. Das, P.D. Howes, A review of laser powder bed fusion additive manufacturing of aluminium alloys: Microstructure and properties, Addit. Manuf. 46 (2021) 102155, http://dx.doi.org/10.1016/j.addma.2021.102155.

[6] R. Bidulský, J. Bidulská, F.S. Gobber, T. Kvačkaj, P. Petroušek, M. Actis-Grande, K.-P. Weiss, D. Manfredi, Case study of the tensile fracture investigation of additive manufactured austenitic stainless steels treated at cryogenic conditions, Materials 13 (15) (2020) 3328, http://dx.doi.org/10.3390/ma13153328.

[7] E.S. Kim, K.R. Ramkumar, G.M. Karthik, S.G. Jeong, S.Y. Ahn, P. Sathiyamoorthi, H. Park, Y.-U. Heo, H.S. Kim, Cryogenic tensile behavior of laser additive manufactured CoCrFeMnNi high entropy alloys, J. Alloys Compd. 942 (2023) 169062, http://dx.doi.org/10.1016/j.jallcom.2023.169062.

[8] S. Lee, K.T. Kim, J.-H. Yu, H.S. Kim, J.W. Bae, J.M. Park, Cryogenic tensile behavior of ferrous medium-entropy alloy additively manufactured by laser powder bed fusion, J. Korean Powder Metall. Inst. 31 (1) (2024) 8–15, http://dx.doi.org/10.4150/KPMI.2024.31.1.8.

[9] H. Park, H. Kwon, K.T. Kim, J.-H. Yu, J. Choe, H. Sung, H.S. Kim, J.G. Kim, J.M. Park, Cryogenic tensile behavior of carbon-doped CoCrFeMnNi high-entropy alloys additively manufactured by laser powder bed fusion, Addit. Manuf. 86 (2024) 104223, http://dx.doi.org/10.1016/j.addma.2024.104223.

[10] J. Radhakrishnan, G. Singh, P. Kumar, N. Nayan, U. Ramamurty, Cryogenic temperature tensile properties of laser powder bed fused Ti-6Al-4V, Materialia 39 (2025) 102307, http://dx.doi.org/10.1016/j.mtla.2024.102307.

[11] B. Xie, W. Zeng, T. Xia, L. Wang, K. Chen, Tailoring the ductility of Ti-6Al-4V titanium alloy fabricated by laser power bed fusion at liquid nitrogen temperature, Coatings 14 (12) (2024) 1528, http://dx.doi.org/10.3390/coatings14121528.

[12] M.F. Khan, R. Ghiaasiaan, P.R. Gradl, S. Shao, N. Shamsaei, Additively manufactured scalmalloy via laser powder bed fusion (L-PBF): temperature-dependent tensile and fatigue behaviors, Fatigue Fract. Eng. Mater. Struct. 48 (4) (2025) 1496–1513, http://dx.doi.org/10.1111/ffe.14549.

[13] S.K. Tumulu, Laser Powder Bed Fusion Additive Manufacturing (LPBF-AM) of Aluminum-Copper Alloys (Ph.D. thesis), McGill University, 2025.

[14] F.T. Inouye, Properties of large 7079 aluminum alloy forgings in a cryogenic environment, 1966.

[15] S. Saji, S. Hori, Mechanical properties of aluminum alloys at very low temperature, J. Light Met. 39 (8) (1989) 574–583, http://dx.doi.org/10.2464/jilm.39.574.

[16] W.A. Monteiro, Light metal alloys applications, in: BoD – Books on Demand, 2014.

[17] R. Schneider, B. Heine, RJ. Grant, Z. Zouaoui, Mechanical behaviour of aircraft relevant aluminium wrought alloys at low temperatures, Proc. Inst. Mech. Eng. Part L: J. Mater.: Des. Appl. 229 (2) (2015) 126–136, http://dx.doi.org/10.1177/1464420713501734.

[18] S. Lee, K. Watanabe, K. Matsuda, Z. Horita, Low-temperature and high-strain-rate superplasticity of ultrafine-grained A7075 processed by high-pressure torsion, Mater. Trans. 59 (8) (2018) 1341–1347, http://dx.doi.org/10.2320/matertrans.L-M2018825.

[19] B. Feng, B. Gu, S. Li, Cryogenic deformation behavior and failure mechanism of AA7075 alloy sheets tempered at different conditions, Mater. Sci. Eng.: A 848 (2022) 143396, http://dx.doi.org/10.1016/j.msea.2022.143396.

[20] B. Feng, B. Gu, S. Li, An efficient pre-hardened cryogenic forming process for AA7075 aluminum alloy sheets, J. Manuf. Process. 92 (2023) 534–547, http://dx.doi.org/10.1016/j.jmapro.2023.02.061.

[21] E.S. Puchi-Cabrera, M.H. Staia, E. Ochoa-Pérez, J.G. La Barbera-Sosa, C. Villalobos-Gutierrez, A. Brenlla-Caires, Flow stress and ductility of AA7075-T6 aluminum alloy at low deformation temperatures, Mater. Sci. Eng.: A 528 (3) (2011) 895–905, http://dx.doi.org/10.1016/j.msea.2010.11.002.

[22] E. Simonetto, R. Bertolini, A. Ghiotti, S. Bruschi, Mechanical and microstructural behaviour of AA7075 aluminium alloy for sub-zero temperature sheet stamping process, Int. J. Mech. Sci. 187 (2020) 105919, http://dx.doi.org/10.1016/j.ijmecsci.2020.105919.

[23] H. Halim, D.S. Wilkinson, M. Niewczas, The Portevin–Le Chatelier (PLC) effect and shear band formation in an AA5754 alloy, Acta Mater. 55 (12) (2007) 4151–4160, http://dx.doi.org/10.1016/j.actamat.2007.03.007.

[24] H. Jiang, Q. Zhang, X. Chen, Z. Chen, Z. Jiang, X. Wu, J. Fan, Three types of Portevin–Le Chatelier effects: Experiment and modelling, Acta Mater. 55 (7) (2007) 2219–2228, http://dx.doi.org/10.1016/j.actamat.2006.10.029.

[25] Z. Xu, H.J. Roven, Z. Jia, Mechanical properties and surface characteristics of an AA6060 alloy strained in tension at cryogenic and room temperature, Mater. Sci. Eng.: A 648 (2015) 350–358, http://dx.doi.org/10.1016/j.msea.2015.09.083.

[26] S. Yuan, W. Cheng, W. Liu, Y. Xu, A novel deep drawing process for aluminum alloy sheets at cryogenic temperatures, J. Mater. Process. Technol. 284 (2020) 116743, http://dx.doi.org/10.1016/j.jmatprotec.2020.116743.

[27] W. Cheng, W. Liu, S. Yuan, Deformation behavior of Al–Cu–Mn alloy sheets under biaxial stress at cryogenic temperatures, Mater. Sci. Eng.: A 759 (2019) 357–367, http://dx.doi.org/10.1016/j.msea.2019.05.047.

[28] F. Dong, Y. Yi, S. Huang, B. Wang, H. He, K. Huang, C. Wang, Cryogenic formability and deformation behavior of 2060 Al–Li alloys with water-quenched and T4 aged temper, Mater. Sci. Eng.: A 823 (2021) 141722, http://dx.doi.org/10.1016/j.msea.2021.141722.

[29] W. Stopyra, K. Gruber, I. Smolina, T. Kurzynowski, B. Kuźnicka, Laser powder bed fusion of AA7075 alloy: Influence of process parameters on porosity and hot cracking, Addit. Manuf. 35 (2020) 101270, http://dx.doi.org/10.1016/j.addma.2020.101270.

[30] M.L. Montero-Sistiaga, R. Mertens, B. Vrancken, X. Wang, B. Van Hooreweder, J.-P. Kruth, J. Van Humbeeck, Changing the alloy composition of Al7075 for better processability by selective laser melting, J. Mater. Process. Technol. 238 (2016) 437–445, http://dx.doi.org/10.1016/j.jmatprotec.2016.08.003.

[31] Y. Otani, Y. Kusaki, K. Itagaki, S. Sasaki, Microstructure and mechanical properties of A7075 alloy with additional Si objects fabricated by selective laser melting, Mater. Trans. 60 (10) (2019) 2143–2150, http://dx.doi.org/10.2320/matertrans.Y-M2019837.

[32] B. Huang, Y. Liu, Z. Zhou, W. Cheng, X. Liu, Selective laser melting of 7075 aluminum alloy inoculated by Al–Ti–B: Grain refinement and superior mechanical properties, Vacuum 200 (2022) 111030, http://dx.doi.org/10.1016/j.vacuum.2022.111030.

[33] B. Fields, M. Amiri, B.E. MacDonald, J.T. Pürstl, C. Dai, X. Li, D. Apelian, L. Valdevit, Investigation of an additively manufactured modified aluminum 7068 alloy: Processing, microstructure, and mechanical properties, Mater. Sci. Eng.: A 891 (2024) 145901, http://dx.doi.org/10.1016/j.msea.2023.145901.

[34] J. Choe, K.T. Kim, J.H. Yu, J.M. Park, D.Y. Yang, S. ho Jung, S. Jo, H. Joo, M. Kang, S.Y. Ahn, S.G. Jeong, E.S. Kim, H. Lee, H.S. Kim, A novel route for predicting the cracking of inoculant-added AA7075 processed via laser powder bed fusion, Addit. Manuf. 62 (2023) 103370, http://dx.doi.org/10.1016/j.addma.2022.103370.

[35] J.H. Martin, B.D. Yahata, J.M. Hundley, J.A. Mayer, T.A. Schaedler, T.M. Pollock, 3D printing of high-strength aluminium alloys, Nature 549 (7672) (2017) 365–369, http://dx.doi.org/10.1038/nature23894.

[36] L. Zhou, H. Pan, H. Hyer, S. Park, Y. Bai, B. McWilliams, K. Cho, Y. Sohn, Microstructure and tensile property of a novel AlZnMgScZr alloy additively manufactured by gas atomization and laser powder bed fusion, Scr. Mater. 158 (2019) 24–28, http://dx.doi.org/10.1016/j.scriptamat.2018.08.025.

[37] L. Zhou, H. Hyer, S. Park, H. Pan, Y. Bai, K.P. Rice, Y. Sohn, Microstructure and mechanical properties of Zr-modified aluminum alloy 5083 manufactured by laser powder bed fusion, Addit. Manuf. 28 (2019) 485–496, http://dx.doi.org/10.1016/j.addma.2019.05.027.

[38] L. Zhou, H. Hyer, S. Thapliyal, R.S. Mishra, B. McWilliams, K. Cho, Y. Sohn, Process-dependent composition, microstructure, and printability of Al-Zn-Mg and Al-Zn-Mg-Sc-Zr alloys manufactured by laser powder bed fusion, Metall. Mater. Trans. A 51 (6) (2020) 3215–3227, http://dx.doi.org/10.1007/s11661-020-05768-3.

[39] Z. Zhu, F.L. Ng, H.L. Seet, W. Lu, C.H. Liebscher, Z. Rao, D. Raabe, S. Mui Ling Nai, Superior mechanical properties of a selective-laser-melted AlZnMgCuScZr alloy enabled by a tunable hierarchical microstructure and dual-nanoprecipitation, Mater. Today 52 (2022) 90–101, http://dx.doi.org/10.1016/j.mattod.2021.11.019.

[40] X. Liu, Y. Liu, Z. Zhou, Q. Zhan, Enhanced strength and ductility in Al-Zn-Mg-Cu alloys fabricated by laser powder bed fusion using a synergistic grain-refining strategy, J. Mater. Sci. Technol. 124 (2022) 41–52, http://dx.doi.org/10.1016/j.jmst.2021.12.078.

[41] M. Lezaack, Fracture of 7xxx Aluminium Alloys with Tailored Friction Stir Processed Microstructures (Ph.D. thesis), 2022.

[42] C. Moon, J. Ma, M.-G. Lee, Dynamics of Portevin-Le Chatelier (PLC) bands and fracture behavior of W-tempered 7075 aluminum alloys with different cooling methods, Mater. Sci. Eng.: A 914 (2024) 147162, http://dx.doi.org/10.1016/j.msea.2024.147162.

[43] N. Nothomb, Microstructure–Property Development in Zr-Modified 7075 Aluminium Alloy Processed By Laser Powder Bed Fusion (Ph. D. thesis), UCLouvain, 2024.

[44] N. Nothomb, I. Rodriguez-Barber, M.-N. Avettand-Fénoël, M.T. Pérez Prado, M. Marinova, A. Simar, Understanding the effect of tailored heat treatment on Zr-modified Al7075 fabricated by laser powder bed fusion, Mater. Des. 258 (2025) 114553, http://dx.doi.org/10.1016/j.matdes.2025.114553.

[45] J.H. Martin, J.E. Barnes, K.A. Rogers, J. Hundley, D.L. LaPlant, S. Ghanbari, J.-T. Tsai, D.F. Bahr, Additive manufacturing of a high-performance aluminum alloy from cold mechanically derived non-spherical powder, Commun. Mater. 4 (1) (2023) 39, http://dx.doi.org/10.1038/s43246-023-00365-4.

[46] N. Nothomb, I. Rodriguez-Barber, M.T. Pérez-Prado, N.J. Mena, G. Pyka, A. Simar, Understanding the effect of pre-sintering scanning strategy on the relative density of Zr-modified Al7075 processed by laser powder bed fusion, Addit. Manuf. Lett. (2024) 100253, http://dx.doi.org/10.1016/j.addlet.2024.100253.

[47] A. Hilhorst, Critical Assessment of the Plasticity and Fracture Properties of High Entropy Alloys Compared To Conventional Alloys (Ph. D. thesis), Université Catholique de Louvain, 2022.

[48] A. Hilhorst, T. Pardoen, P.J. Jacques, Optimization of the essential work of fracture method for characterization of the fracture resistance of metallic sheets, Eng. Fract. Mech. 268 (2022) 108442, http://dx.doi.org/10.1016/j.engfracmech.2022.108442.

[49] J.A. Huwaldt, Plot digitizer, 2020.

[50] A. Simar, K. Nielsen, B. De Meester, V. Tvergaard, T. Pardoen, Micro-mechanical modelling of ductile failure in 6005A aluminium using a physics based strain hardening law including stage IV, Eng. Fract. Mech. 77 (13) (2010) 2491–2503, http://dx.doi.org/10.1016/j.engfracmech.2010.06.008.

[51] F. Bachmann, R. Hielscher, H. Schaeben, Grain detection from 2d and 3d EBSD data—Specification of the MTEX algorithm, Ultramicroscopy 111 (12) (2011) 1720–1733, http://dx.doi.org/10.1016/j.ultramic.2011.08.002.

[52] J. Schindelin, I. Arganda-Carreras, E. Frise, V. Kaynig, M. Longair, T. Pietzsch, S. Preibisch, C. Rueden, S. Saalfeld, B. Schmid, J.-Y. Tinevez, D.J. White, V. Hartenstein, K. Eliceiri, P. Tomancak, A. Cardona, Fiji: An open-source platform for biological-image analysis, Nature Methods 9 (7) (2012) 676–682, http://dx.doi.org/10.1038/nmeth.2019.

[53] L. Cabrera-Correa, L. González-Rovira, J. de Dios López-Castro, M. Castillo-Rodríguez, F.J. Botana, Effect of the heat treatment on the mechanical properties and microstructure of Scalmalloy® manufactured by Selective Laser Melting (SLM) under certified conditions, Mater. Charact. 196 (2023) 112549, http://dx.doi.org/10.1016/j.matchar.2022.112549.

[54] G. Simmons, H. Wang, Single Crystal Elastic Constants and Calculated Aggregare Properties : A Handbook, The Mit Press Edition, 1971.

[55] Y. Luo, N. Nothomb, T. Yu, L. Zhao, J. Villanova, Z. Li, A. Simar, Effects of microstructure heterogeneity and defects on mechanical behavior of Zr modified AA7075 manufactured by laser powder bed fusion, Addit. Manuf. 97 (2025) 104626, http://dx.doi.org/10.1016/j.addma.2024.104626.

[56] A. Mehta, L. Zhou, T. Huynh, S. Park, H. Hyer, S. Song, Y. Bai, D.D. Imholte, N.E. Woolstenhulme, D.M. Wachs, Y. Sohn, Additive manufacturing and mechanical properties of the dense and crack free Zr-modified aluminum alloy 6061 fabricated by the laser-powder bed fusion, Addit. Manuf. 41 (2021) 101966, http://dx.doi.org/10.1016/j.addma.2021.101966.

[57] G. Kermouche, J. Loubet, J. Bergheau, Extraction of stress–strain curves of elastic–viscoplastic solids using conical/pyramidal indentation testing with application to polymers, Mech. Mater. 40 (4–5) (2008) 271–283, http://dx.doi.org/10.1016/j.mechmat.2007.08.003.

[58] V. Alfieri, V. Giannella, F. Caiazzo, R. Sepe, Influence of position and building orientation on the static properties of LPBF specimens in 17-4 PH stainless steel, Forces Mech. 8 (2022) 100108, http://dx.doi.org/10.1016/j.finmec.2022.100108.

[59] A. Mussatto, R. Groarke, R.K. Vijayaraghavan, C. Hughes, M.A. Obeidi, M.N. Doğu, M.A. Yalçin, P.J. McNally, Y. Delaure, D. Brabazon, Assessing dependency of part properties on the printing location in laser-powder bed fusion metal additive manufacturing, Mater. Today Commun. 30 (2022) 103209, http://dx.doi.org/10.1016/j.mtcomm.2022.103209.

[60] M. Simonelli, Y.Y. Tse, C. Tuck, Effect of the build orientation on the mechanical properties and fracture modes of SLM Ti–6Al–4V, Mater. Sci. Eng.: A 616 (2014) 1–11, http://dx.doi.org/10.1016/j.msea.2014.07.086.

[61] J. Suryawanshi, K.G. Prashanth, S. Scudino, J. Eckert, O. Prakash, U. Ramamurty, Simultaneous enhancements of strength and toughness in an Al-12Si alloy synthesized using selective laser melting, Acta Mater. 115 (2016) 285–294, http://dx.doi.org/10.1016/j.actamat.2016.06.009.

[62] J. Tang, R. Wróbel, P. Scheel, W. Gaechter, C. Leinenbach, E. Hosseini, The role of process parameters and printing position on meltpool variations in LPBF Hastelloy X: Insights into laser-plume interaction, Addit. Manuf. Lett. 9 (2024) 100203, http://dx.doi.org/10.1016/j.addlet.2024.100203.

[63] Y. Shi, K. Yang, S.K. Kairy, F. Palm, X. Wu, P.A. Rometsch, Effect of platform temperature on the porosity, microstructure and mechanical properties of an Al–Mg–Sc–Zr alloy fabricated by selective laser melting, Mater. Sci. Eng.: A 732 (2018) 41–52, http://dx.doi.org/10.1016/j.msea.2018.06.049.

[64] R.A. Michi, A. Plotkowski, A. Shyam, R.R. Dehoff, S.S. Babu, Towards high-temperature applications of aluminium alloys enabled by additive manufacturing, Int. Mater. Rev. 67 (3) (2022) 298–345, http://dx.doi.org/10.1080/09506608.2021.1951580.

[65] K. Johnson, Contact Mechanics, Cambridge University Press, 1987.

[66] D. Caillard, J.-L. Martin, Thermally activated mechanisms in crystal plasticity, Pergamon Materials Series, Pergamon, Amsterdam, Boston, Mass, 2003, no. 8.

[67] P. Follansbee, U. Kocks, A constitutive description of the deformation of copper based on the use of the mechanical threshold stress as an internal state variable, Acta Metall. 36 (1) (1988) 81–93, http://dx.doi.org/10.1016/0001-6160(88)90030-2.

[68] P.S. Follansbee, Development and application of an internal state variable constitutive model for deformation of metals, J. Mater. Res. Technol. 36 (2025) 284–291, http://dx.doi.org/10.1016/j.jmrt.2025.03.062.

[69] J. Jonas, The back stress in high temperature deformation, Acta Metall. 17 (4) (1969) 397–405, http://dx.doi.org/10.1016/0001-6160(69)90020-0.

[70] J. Klepaczko, Thermally activated flow and strain rate history effects for some polycrystalline f.c.c. metals, Mater. Sci. Eng. 18 (1) (1975) 121–135, http://dx.doi.org/10.1016/0025-5416(75)90078-6.

[71] R. Labusch, A statistical theory of solid solution hardening, Phys. Status Solidi (B) 41 (2) (1970) 659–669, http://dx.doi.org/10.1002/pssb.19700410221.

[72] G.P.M. Leyson, W.A. Curtin, L.G. Hector, C.F. Woodward, Quantitative prediction of solute strengthening in aluminium alloys, Nat. Mater. 9 (9) (2010) 750–755, http://dx.doi.org/10.1038/nmat2813.

[73] G.P.M. Leyson, L.G. Hector, W.A. Curtin, Solute strengthening from first principles and application to aluminum alloys, Acta Mater. 60 (9) (2012) 3873–3884, http://dx.doi.org/10.1016/j.actamat.2012.03.037.

[74] G.P.M. Leyson, W.A. Curtin, Solute strengthening at high temperatures, Modelling Simul. Mater. Sci. Eng. 24 (6) (2016) 065005, http://dx.doi.org/10.1088/0965-0393/24/6/065005.

[75] D. Ma, M. Friák, J. von Pezold, D. Raabe, J. Neugebauer, Ab initio identified design principles of solid-solution strengthening in Al, Sci. Technol. Adv. Mater. 14 (2) (2013) 025001, http://dx.doi.org/10.1088/1468-6996/14/2/025001.

[76] D. Ma, M. Friák, J. Von Pezold, D. Raabe, J. Neugebauer, Computationally efficient and quantitatively accurate multiscale simulation of solid-solution strengthening by ab initio calculation, Acta Mater. 85 (2015) 53–66, http://dx.doi.org/10.1016/j.actamat.2014.10.044.

[77] A. Seeger, The temperature dependence of the critical shear stress and of work-hardening of metal crystals, Lond. Edinb. Dublin Philos. Mag. J. Sci. 45 (366) (1954) 771–773, http://dx.doi.org/10.1080/14786440708520489.

[78] A. Seeger, LXV. On the theory of the low-temperature internal friction peak observed in metals, Phil. Mag. 1 (7) (1956) 651–662, http://dx.doi.org/10.1080/14786435608244000.

[79] G. Sun, M. Lei, S. Liu, B. Wen, Orowan strengthening with consideration of thermal activation, Comput. Mater. Sci. 233 (2024) 112720, http://dx.doi.org/10.1016/j.commatsci.2023.112720.

[80] G. Sun, L. Zhang, B. Wen, Thermally-activated precipitation strengthening, J. Mater. Res. Technol. 29 (2024) 2131–2141, http://dx.doi.org/10.1016/j.jmrt.2024.01.291.

[81] J.A. Yasi, L.G. Hector, D.R. Trinkle, First-principles data for solid-solution strengthening of magnesium: From geometry and chemistry to properties, Acta Mater. 58 (17) (2010) 5704–5713, http://dx.doi.org/10.1016/j.actamat.2010.06.045.

[82] H. Hyer, A. Mehta, K. Graydon, N. Kljestan, M. Knezevic, D. Weiss, B. McWilliams, K. Cho, Y. Sohn, High strength aluminum-cerium alloy processed by laser powder bed fusion, Addit. Manuf. 52 (2022) 102657, http://dx.doi.org/10.1016/j.addma.2022.102657.

[83] K. Ma, H. Wen, T. Hu, T.D. Topping, D. Isheim, D.N. Seidman, E.J. Lavernia, J.M. Schoenung, Mechanical behavior and strengthening mechanisms in ultrafine grain precipitation-strengthened aluminum alloy, Acta Mater. 62 (2014) 141–155, http://dx.doi.org/10.1016/j.actamat.2013.09.042.

[84] L.D. Landau, E.M. Lifshitz, Theory of elasticity, second ed., in: Course of Theoretical Physics, vol. 7, Oxford, Pergamon, 1970.

[85] S. Gao, K. Yoshino, D. Terada, Y. Kaneko, N. Tsuji, Significant Bauschinger effect and back stress strengthening in an ultrafine grained pure aluminum fabricated by severe plastic deformation process, Scr. Mater. 211 (2022) 114503, http://dx.doi.org/10.1016/j.scriptamat.2022.114503.

[86] Y. Guo, W. Wei, W. Shi, X. Zhou, S. Wen, X. Wu, K. Gao, D. Zhang, P. Qi, H. Huang, Z. Nie, Microstructure and mechanical properties of Al-Mg-Mn-Er-Zr alloys fabricated by laser powder bed fusion, Mater. Des. 222 (2022) 111064, http://dx.doi.org/10.1016/j.matdes.2022.111064.

[87] Q. Jia, P. Rometsch, P. Kürnsteiner, Q. Chao, A. Huang, M. Weyland, L. Bourgeois, X. Wu, Selective laser melting of a high strength AlMnSc alloy: Alloy design and strengthening mechanisms, Acta Mater. 171 (2019) 108–118, http://dx.doi.org/10.1016/j.actamat.2019.04.014.

[88] R.A. Austin, D.L. McDowell, A dislocation-based constitutive model for viscoplastic deformation of fcc metals at very high strain rates, Int. J. Plast. 27 (1) (2011) 1–24, http://dx.doi.org/10.1016/j.ijplas.2010.03.002.

[89] K.E. Knipling, R.A. Karnesky, C.P. Lee, D.C. Dunand, D.N. Seidman, Precipitation evolution in Al–0.1Sc, Al–0.1Zr and Al–0.1Sc–0.1Zr (at. %) alloys during isochronal aging, Acta Mater. 58 (15) (2010) 5184–5195, http://dx.doi.org/10.1016/j.actamat.2010.05.054.

[90] J.D. Robson, P.B. Prangnell, Modelling Al3Zr dispersoid precipitation in multicomponent aluminium alloys, Mater. Sci. Eng.: A 352 (1) (2003) 240–250, http://dx.doi.org/10.1016/S0921-5093(02)00894-8.

[91] C. Sigli, Zirconium solubility in aluminum alloys.

[92] A.Y. Algendy, K. Liu, P. Rometsch, N. Parson, X.G. Chen, Effects of AlMn dispersoids and Al3(Sc,Zr) precipitates on the microstructure and ambient/elevated-temperature mechanical properties of hot-rolled AA5083 alloys, Mater. Sci. Eng.: A 855 (2022) 143950, http://dx.doi.org/10.1016/j.msea.2022.143950.

[93] E. Pourkhorshid, M.H. Enayati, S. Sabooni, F. Karimzadeh, M.H. Paydar, Bulk Al–Al3Zr composite prepared by mechanical alloying and hot extrusion for high-temperature applications, Int. J. Miner. Metall. Mater. 24 (8) (2017) 937–942, http://dx.doi.org/10.1007/s12613-017-1481-7.

[94] A. Martin, M. Vilanova, E. Gil, M.S. Sebastian, C.Y. Wang, S. Milenkovic, M.T. Pérez-Prado, C.M. Cepeda-Jiménez, Influence of the Zr content on the processability of a high strength Al-Zn-Mg-Cu-Zr alloy by laser powder bed fusion, Mater. Charact. 183 (2022) 111650, http://dx.doi.org/10.1016/j.matchar.2021.111650.

[95] S. Fu, Q. Zhang, Q. Hu, M. Gong, P. Cao, H. Liu, The influence of temperature on the PLC effect in Al-Mg alloy, Sci. China Technol. Sci. 54 (6) (2011) 1389–1393, http://dx.doi.org/10.1007/s11431-011-4398-9.

[96] M. Jobba, R.K. Mishra, M. Niewczas, Flow stress and work-hardening behaviour of Al–Mg binary alloys, Int. J. Plast. 65 (2015) 43–60, http://dx.doi.org/10.1016/j.ijplas.2014.08.006.

[97] C.Y. Yu, P.W. Kao, C.P. Chang, Transition of tensile deformation behaviors in ultrafine-grained aluminum, Acta Mater. 53 (15) (2005) 4019–4028, http://dx.doi.org/10.1016/j.actamat.2005.05.005.

[98] F. Czerwinski, Thermal stability of aluminum alloys, Materials 13 (15) (2020) 3441, http://dx.doi.org/10.3390/ma13153441.

[99] D.J. Lloyd, The deformation of commercial aluminum-magnesium alloys, Metall. Trans. A 11 (8) (1980) 1287–1294, http://dx.doi.org/10.1007/BF02653482.

[100] W. Wen, J.G. Morris, The effect of cold rolling and annealing on the serrated yielding phenomenon of AA5182 aluminum alloy, Mater. Sci. Eng.: A 373 (1) (2004) 204–216, http://dx.doi.org/10.1016/j.msea.2004.01.041.

[101] Y. Geng, D. Zhang, J. Zhang, L. Zhuang, On the suppression of Lüders elongation in high-strength Cu/Zn modified 5xxx series aluminum alloy, J. Alloys Compd. 834 (2020) 155138, http://dx.doi.org/10.1016/j.jallcom.2020.155138.

[102] M. Buttard, B. Chéhab, C. Josserond, F. Charlot, P. Lhuissier, X. Bataillon, A. Deschamps, J. Villanova, M. Fivel, J.-J. Blandin, G. Martin, Influence of microstructure heterogeneity on the tensile response of an Aluminium alloy designed for laser powder bed fusion, Acta Mater. 269 (2024) 119786, http://dx.doi.org/10.1016/j.actamat.2024.119786.

[103] G. Li, E. Brodu, J. Soete, H. Wei, T. Liu, T. Yang, W. Liao, K. Vanmeensel, Exploiting the rapid solidification potential of laser powder bed fusion in high strength and crack-free Al-Cu-Mg-Mn-Zr alloys, Addit. Manuf. 47 (2021) 102210, http://dx.doi.org/10.1016/j.addma.2021.102210.

[104] D. Bayoumy, K. Kwak, T. Boll, S. Dietrich, D. Schliephake, J. Huang, J. Yi, K. Takashima, X. Wu, Y. Zhu, A. Huang, Origin of non-uniform plasticity in a high-strength Al-Mn-Sc based alloy produced by laser powder bed fusion, J. Mater. Sci. Technol. 103 (2022) 121–133, http://dx.doi.org/10.1016/j.jmst.2021.06.042.

[105] N. Tsuchida, Y. Tomota, K. Nagai, K. Fukaura, A simple relationship between Lüders elongation and work-hardening rate at lower yield stress, Scr. Mater. 54 (1) (2006) 57–60, http://dx.doi.org/10.1016/j.scriptamat.2005.09.011.

[106] A. Deschamps, M. Militzer, W.J. Poole, Precipitation kinetics and strengthening of a Fe–0.8wt%Cu alloy, ISIJ Int. 41 (2) (2001) 196–205, http://dx.doi.org/10.2355/isijinternational.41.196.

[107] V. Ballarin, M. Soler, A. Perlade, X. Lemoine, S. Forest, Mechanisms and modeling of bake-hardening steels: Part I, uniaxial tension, Metall. Mater. Trans. A 40 (6) (2009) 1367–1374, http://dx.doi.org/10.1007/s11661-009-9813-5.

[108] H.J. Kong, T. Yang, R. Chen, S.Q. Yue, T.L. Zhang, B.X. Cao, C. Wang, W.H. Liu, J.H. Luan, Z.B. Jiao, B.W. Zhou, L.G. Meng, A. Wang, C.T. Liu, Breaking the strength-ductility paradox in advanced nanostructured Fe-based alloys through combined Cu and Mn additions, Scr. Mater. 186 (2020) 213–218, http://dx.doi.org/10.1016/j.scriptamat.2020.05.008.

[109] D.H. Johnson, LÜders Bands in RPV Steel (Ph. D. thesis), Cranfield University, 2012.

[110] CM. Sellars, W.M. Tegart, Hot workability, Int. Metall. Rev. 17 (1) (1972) 1–24.

[111] M. Arseenko, F. Hannard, L. Ding, L. Zhao, E. Maire, J. Villanova, H. Idrissi, A. Simar, A new healing strategy for metals: Programmed damage and repair, Acta Mater. 238 (2022) 118241, http://dx.doi.org/10.1016/j.actamat.2022.118241.

[112] M. Arseenko, J. Gheysen, F. Hannard, N. Nothomb, A. Simar, Self-healing in metal-based systems, in: A. Kanellopoulos, J. Norambuena-Contreras (Eds.), Self-Healing Construction Materials: Fundamentals, Monitoring and Large Scale Applications, Springer International Publishing, Cham, 2022, pp. 43–78, http://dx.doi.org/10.1007/978-3-030-86880-2_3.

[113] A. Kashiwar, M. Arseenko, A. Simar, H. Idrissi, On the role of microstructural defects on precipitation, damage, and healing behavior in a novel Al-0.5Mg2Si alloy, Mater. Des. 239 (2024) 112765, http://dx.doi.org/10.1016/j.matdes.2024.112765.

[114] J. Besson, D. Steglich, W. Brocks, Modeling of plane strain ductile rupture, Int. J. Plast. 19 (10) (2003) 1517–1541, http://dx.doi.org/10.1016/S0749-6419(02)00022-0.

[115] A. Pineau, A.A. Benzerga, T. Pardoen, Failure of metals I: Brittle and ductile fracture, Acta Mater. 107 (2016) 424–483, http://dx.doi.org/10.1016/j.actamat.2015.12.034.